The Deformation Law of a Soft-Rock Cavern by Step Excavation in a Pumped Storage Power Station

Ning Sun [1], Xiaokai Li [2], Shanggao Li [1], Dake Hu [1], Mengjiao Hu [1], Faming Zhang [2], Yiyan Zhong [2], Menglong Dong [2] and Zinan Li [2,*]

1   Zhongnan Engineering Corporation Limited, Power China, Changsha 410014, China
2   School of Earth Science and Engineering, Hohai University, Nanjing 211100, China
*   Correspondence: lizinan@hhu.edu.cn

Abstract: The surrounding rock stability of large underground caverns in a pumped storage power station is one of the most crucial problems in hydropower project design and construction. In the construction of hydropower projects in Southwest China, many underground soft-rock caverns in are excavated. Influenced by the high sidewall, high ground stress, large burial depth, and hydrodynamic pressure action, the deformation of the cavern is special, especially in terms of its soft-rock distribution. At present, most research of underground engineering on soft-rock stability focuses on small-scale tunnel excavations in homogeneous geological conditions, with limited studies on the large-scale excavation of deeply buried underground powerhouses in complex geological structures, featuring extensive soft-rock-layer exposure on the cavern wall. Therefore, it is particularly important to investigate the excavation method of and support measures for soft-rock caverns under complex geological conditions. Based on laboratory rock mechanics testing (petrographic analysis, uniaxial compressive strength tests, shear tests, and triaxial compression creep tests) and the distribution characteristics of the surrounding soft-rock layer of the proposed underground powerhouse, obtained from the survey, we discuss the excavation and support measurements. These include the influence of support measures on the deformation of the underground excavated cavern considering the inclination of rock layers, the impact of the excavation under supported conditions on the deformation of the underground cavern, and the correlation between the lining thickness and stress variation within the lining.

1. Introduction

Groundwater conveyance and power generation systems form the core of hydropower stations. Therefore, during the construction of a hydroelectric power station, studying the stability of the surrounding rock of large underground cavern groups is one of the most important aspects of the project. With the advancement of hydropower projects, the geological conditions encountered during underground powerhouse excavations are becoming increasingly complex, and the issue of the large deformation of soft rock is becoming increasingly prominent.

There are several studies on the large deformation of soft rock in underground engineering. The stability of soft-rock caverns is influenced by various factors, including the shape and size of the underground excavation space, the geological structure and characteristics, excavation procedures, support measures, and the deformation characteristics of different soft rocks. Zhao and Ma discussed the effect of spacing between caverns on the stability of adjacent caverns [1]. Huang et al. proposed that the cavern shrinkage rate was influenced by the thickness of the soft- and hard-rock layers [2].

Xue et al. proposed a surrounding rock classification model based on the weights back analysis and efficiency method, which considers rock compressive strength, integrated coefficient, the character of discontinuity, groundwater, and the angle between the tunnel axis and soft surface [3]. Tsearsky et al. performed a stability analysis on the local-discontinuous and global-continuous scales of underground openings in soft- and discontinuous rock masses [4]. Zhou et al. used an underground water-sealed gas storage cavern as an example to analyze the main controlling factors of blasting vibrations on the deformation of the surrounding rock [5]. Lu and Sun considered the enhancement effect of the intermediate principal stress on rock strength and provided theoretical answers to the optimal support force and maximum allowable displacement of the surrounding rock in soft-rock caverns [6]. Zhang et al. conducted true three-dimensional geological mechanics model tests for layered, jointed rock masses with weak interlayers, based on the background of deep excavated coal mine roadways [7]. Mortazavi and Nasab discussed the cavern size and depth, deformation modulus, and ground in situ stress on the deformation of large salt caverns [8]. Zhang et al. discussed the influence of interlayers in a bedded salt formation on the stability of salt caverns and proposed that the salt cavern should be constructed away from the interlayers [9,10]. Sun et al. conducted physical simulation experiments on the deformation mechanism of deep-buried tunnels, suggesting that excavation advance and bedding planes would affect the deformation of the surrounding rock [11]. Liu et al. explored the deformation evolution distribution law and failure mechanisms of the surrounding rock of a high side wall of the left bank underground powerhouse of Baihetan Dam [12]. Merlini et al. used the long Ceneri Base Tunnel as an example to introduce excavation and support measures encountered in tunnel engineering [13]. Meng et al. proposed a new classification method for stress-bearing structures in deep-buried roadways [14]. Wang et al. proposed a calculation method for the surrounding soft rock of underground caverns considering the multirigidity slider translation and rotation failure mode [15]. Rybak et al. discussed the influence of backfilling on the dynamics of the deformation of the undermined rock mass [16]. Dyduch et al. discussed the support measures in the Wieliczka salt mine [17]. Li et al. investigated the application of the prestressed anchoring system in soft-rock tunnels, establishing that the key control factors were pre-stress, anchor cable length, and anchor cable spacing [18]. Zheng et al., with a case study of a crossover cavern in Los Angeles, discussed the impact of excavation and support construction steps on the surrounding rocks' stability [19]. Jaroslav et al. discussed the definition of the influence of stowing on the dynamics of the deformation of underworked rock mass [20]. Sari analyzed a storage cavern in Tukey's Cappadocia by 2D and 3D finite-element methods, and proposed that, at the same location, 2D and 3D stability results were different [21]. Yang et al. proposed a soft-rock quality classification method considering the influence of groundwater [22]. Xie et al. discussed the support issues of a deep super-large section soft-rock chamber group, divided it into different control areas based on various deformation volumes, and applied different reinforcement methods [23]. Cui et al. proposed a unified expression for soft rock to evaluate the elastic modulus with the coupling effect of the plastic strain and confining stress [24]. Chen et al. conducted an analysis using the whole coal cavern group as the object, describing the asymmetric failure character of the surrounding rock and analyzing the stratified reinforcement ring support method of long cable-bolt grouting [25]. Mahmoudi and Rajabi used the finite difference method to discuss the influence of concealed kartic caves on the stability of adjacent tunnels [26]. Meanwhile, the research related to soft-rock creep, which is needed for simulation calculations, indicated that the moisture content and the surrounding rock significantly affected the creep behavior of rocks [27,28]. Tang et al. concluded that the creep effect of loess intensified with the increase in moisture content and reduced with the increase in the surrounding rock [29]. Through experiments on mudstone, Liu et al. found that moisture content and deviatoric stress markedly influenced the creep behavior of weakly cemented soft rocks [30]. Wang et al. determined, through creep tests on coal rocks, that coal's creep strain and deformation rate were particularly sensitive to the confining pressure within a certain range [31].

According to the aforementioned research, the study of the stability of soft rock in underground engineering has increasingly attracted scholars' attention. However, prior studies have mainly been conducted on a smaller scale, focusing on the stability of soft-rock tunnels. A reduced amount of research has been conducted on the stability of large-scale deeply buried underground cavern groups where a substantial layer of soft rock (>10 m) is exposed on the cavern wall. Given that the rheological characteristics of soft rock are influenced by soft-rock type, confining pressure, and water content, conducting tests based on undisturbed samples and subsequently drawing conclusions for related numerical analyses are of paramount importance.

In this paper, the excavation of the proposed underground caverns of the Liziwan Hydropower Station is taken as an example. In this case, we discuss the impact of excavation support on the stability of the cavern's surrounding rock under complex compound geological conditions a substantial layer of soft rock is exposed on the cavern walls. This study offers practical and effective suggestions for subsequent excavation steps, providing a valuable reference for the excavation of similar projects.

2. Methodology

This paper used the Liziwan Pumped Storage Power Station, in Chongqing, China, as an example to use the finite difference method to explore the deformation law of the underground cavern, whose surrounding rock is mainly composed of soft rocks. Based on laboratory rock mechanics testing (petrographic analysis, uniaxial compressive strength tests, shear tests, and triaxial compression creep tests) and the distribution characteristics of the surrounding soft-rock layer of the proposed underground cavern, obtained from the survey, discussions were held on excavation and support measurements topics. These included the influence of support measures on the deformation of the underground excavated cavern considering the inclination of rock layers, the impact of the excavation advance under supported conditions on the deformation of the underground cavern, and the correlation between lining thickness and stress variation within the lining.

2.1. Laboratory Rock Mechanics Testing

2.1.1. Rock Chemical Composition and Mineral Constituents

Samples were obtained from within the study area and ground into thin sections with a thickness of 0.3 mm for a petrographic analysis. A polarizing microscope was used to observe the samples; identify the mineral composition, structure, and texture of the rocks; and name the samples.

2.1.2. Uniaxial Compressive Strength and Shear Tests

Through multiple sets of uniaxial compressive strength and shear tests, related rock mechanics tests were conducted on the mudstone and sandstone in the study area. The shear fracture test of the rock was conducted using the direct shear method, where the sample was placed in a shear box, and the gap between the specimen and inner wall of the shear box was filled with fillers. After the sample was sheared and failed, the shear and normal loads were reduced to zero, and the shear test was conducted again.

2.1.3. Triaxial Compression Creep Test

The FSTX-100 frozen soil dynamic and static triaxial apparatus developed and produced by GCTS Company in the United States were selected for the experiment, as shown in Figure 1a. This testing machine was mainly composed of five parts: a dynamic loading frame, pressure instrument, servo control-mode system, temperature control system, and hydraulic pump station. It can complete static, stress path, and dynamic tests (liquefaction strength, modulus/damping measurement, dynamic strength, and rebound modulus, etc.) for three testing methods (unconsolidated undrained, consolidated undrained, and consolidated drained). Its technical specifications were: static load range $\pm$ 100 KN, accuracy 0.05%; the maximum axial displacement was 100 mm; the confining pressure range was

0–20 MPa, with an accuracy of 0.25%; and the temperature control range was −30 °C to +80 °C, with a fluctuation of ±0.1 °C. The testing process was completely controlled by a computer and data collection was automatic; the local displacement sensor is shown in Figure 1b. The test steps are shown below.
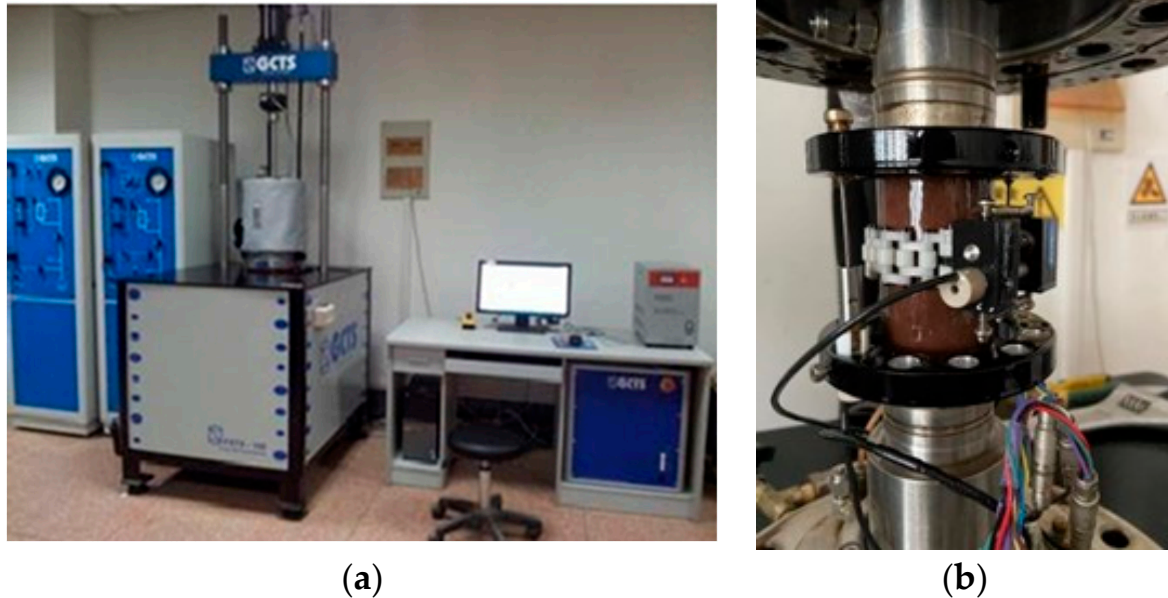

(a)

(b)

Figure 1. Triaxial compression creep test equipment and system. (**a**) FSTX-100 dynamic and static triaxial instruments; (**b**) local displacement sensor.

1. Based on the conventional compressive strength test results of the rock samples at the same sampling point, determine the incremental loading under each lateral pressure and use the Chen's compression method to load in five stages;
2. Load the axial and lateral pressures at a loading rate of 0.05 MPa/s to the predetermined lateral pressure, and load the axial pressure at a rate of 0.2–0.5 MPa/s to the predetermined axial pressure, while collecting the stress and strain values;
3. During the testing process, the automatic collection and storage of the pressure and strain values should be conducted. The data collection interval should not be longer than 5 min in the early stage of the experiment; during the deceleration creep stage, the data collection interval should not be longer than 30 min. The stability standard for each level of loading was a displacement less than 0.001 mm/h or a specified duration.
4. Based on the relationship curve between the axial strain, radial strain, and time, fit and determine the triaxial compression creep model and parameters of rocks.

2.2. Numerical Analysis

2.2.1. Characteristics of Soft-Rock Mass

According to the site's geological investigation data, the surrounding layers of the proposed chamber are shown in Figure 2, whose integrity was good. The main surrounding layers were sandstone and mudstone. Among them, the sandstone layer had high strength, while mudstone and silty mudstone were characterized by low strength, low modulus of deformation, and poor deformation resistance. Moreover, exists mudstone, sandy mudstone, and muddy sandstone with a thickness of up to 30 m were evident.
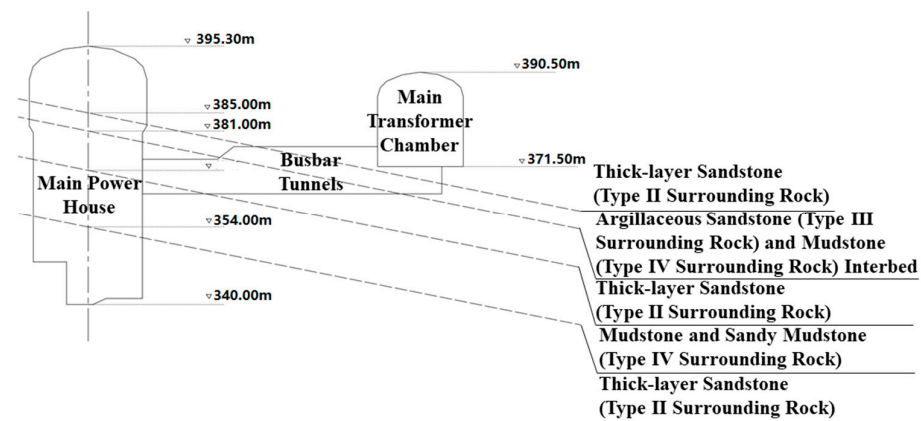
Figure 2. Surrounding rock distribution at main powerhouse at pumped storage power station.

Soft rock produces obvious plastic deformation due to its soft cement or a large number of structural planes. Through laboratory tests and field data analysis, it was concluded that the engineering properties of soft rock mainly included plasticity, expansibility, easy disintegration, and rheology.

2.2.2. Geometric Model

According to the design of the pumped storage power station, there was one main power house, one main transformer chamber, and five busbar tunnels, which connected the main power house and main transformer chamber. The shape of the main power house and main transformer chamber was rectangular with an arch crown, with a length of 171.0 m and a width of 27.5 m for the main power house and a length of 156.0 m and a width of 20.0 m for the main transformer chamber. The whole model was 530.0 m in length, 300.0 m in width, and 250.0~350.0 m in height, consisting of two types of layers: sandstone and mudstone. Details of the model are shown in Figure 3. It is necessary to emphasize that the actual carven was buried at a 500 m depth; for the purpose of an easy calculation, the weight of upper layer was transformed as stress was applied to the top layer of the model.
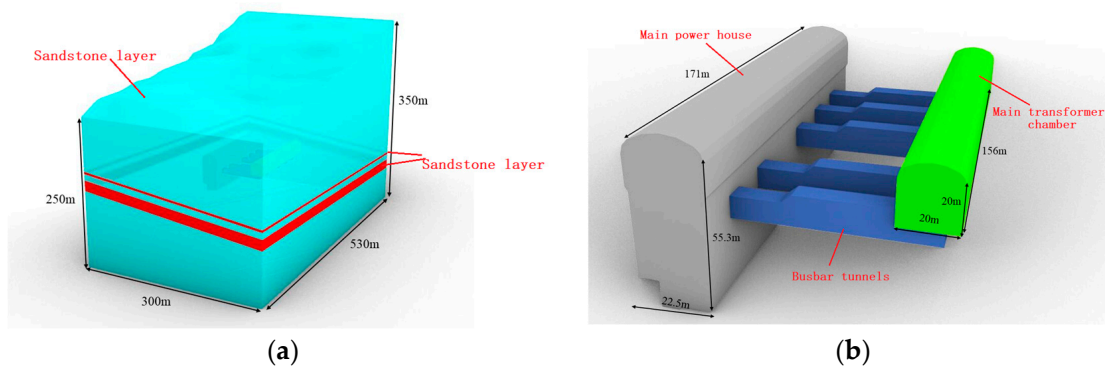

(**a**)

(**b**)

Figure 3. Geometric model. (**a**) Overall geometric model; (**b**) underground cavern model.

2.2.3. The Numerical Model for Comparing Support Effectiveness

Based on the data obtained from the laboratory tests, the sandstone layer was assigned using the Mohr–Coulomb model, and the mudstone layer was assigned the Burgers–Mohr–Coulomb model for calculations. According to the designed excavation steps of the underground cavern, the excavation of any cross-section was completed from the 1st to the 11th step, with a total of 11 steps. The excavation step time for the Burgers–Mohr–Coulomb model was arranged as follows: the excavation time for each step was 60 days, the excavation was completed after 660 days, and the calculation results 365 days after the completion of the excavation were obtained as the object for the displacement analysis. The

numerical models consisted of one supported model and one unsupported model, with consistent excavation step times in both. In the supported model, anchor bolts and lining were applied for support after each excavation step. The layout of the anchor bolts are shown in Figure 4. The lining was established on the free face after the excavation. The parameters for the anchor bolts can be found in Table 1. The elastic modulus of the lining was 3.4×10^{-4} MPa, the Poisson's ratio of the lining was 0.2, and the thickness of the lining was 0.5 m.
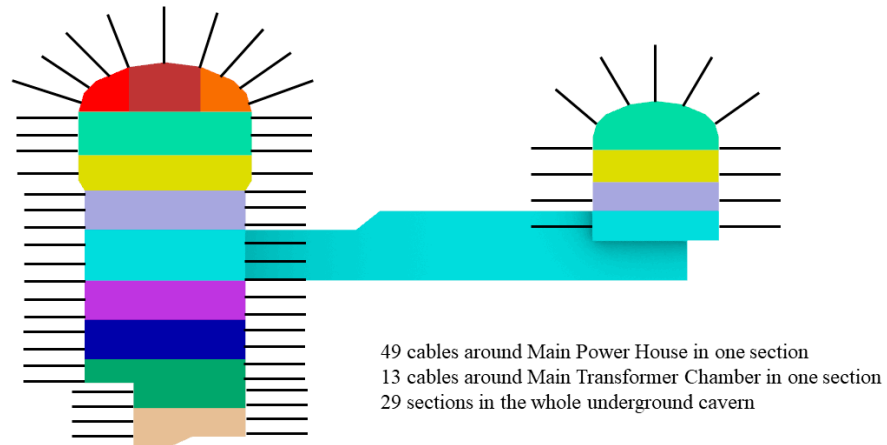

49 cables around Main Power House in one section
13 cables around Main Transformer Chamber in one section
29 sections in the whole underground cavern

Figure 4. Layout of the anchor bolts.

Table 1. Anchor parameters.

Support Type	Elastic Modulus (MPa)	Cross-Sectional Area (m^2)	Tensile Strength (GPa)	Anchor Length (m)
Anchor	2.0×10^5	1.4×10^{-4}	4.90×10^2	9

For the boundary conditions, at the bottom of the model, the displacements in X, Y, and Z directions were fixed, the displacement in the X direction was limited at the left and right sides of the model, and the displacement in the Y direction was limited at the front and back of the model. The details of the model are shown in Figure 5.
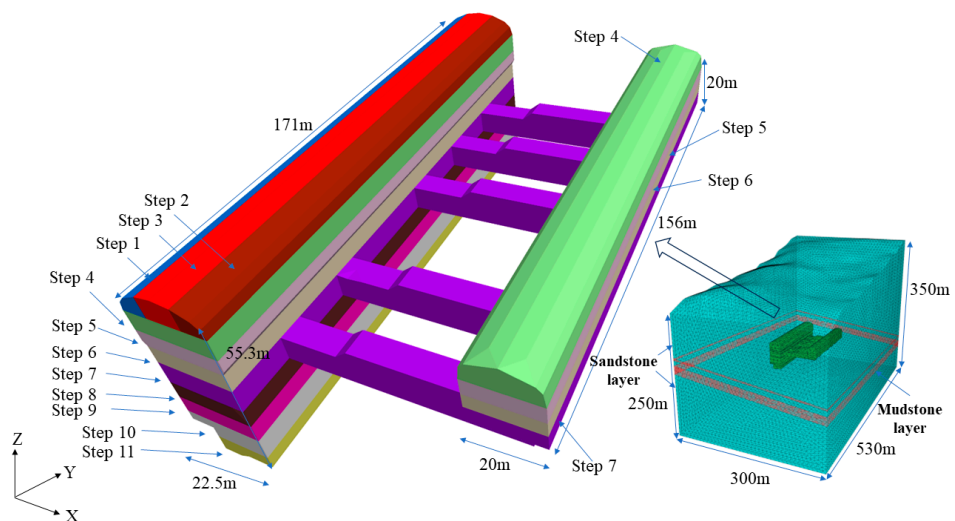

Figure 5. Excavation model.

For the layout of the monitoring points, three monitoring surfaces were arranged in the front, middle, and rear sections of the tunnel, which were arranged at 26, 92, and

144 m distances of the tunnel footage. A total of 30 monitoring points were arranged around the main power house, 15 monitoring points were arranged on the tunnel wall, and 15 monitoring points were arranged extending 5 m to the surrounding rock of the tunnel (Figure 6).
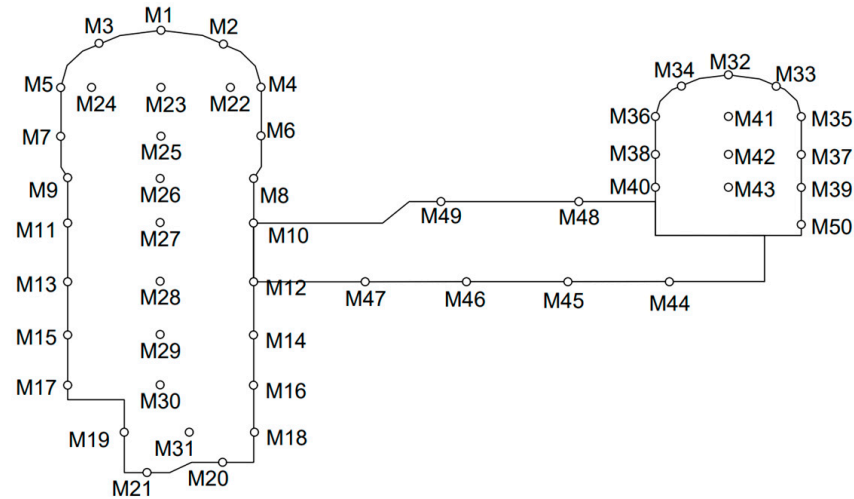

Figure 6. The layout of the monitoring points.

2.2.4. The Numerical Model for Discussing the Effect of the Excavation Advance on the Deformation of the Surrounding Soft Rock

Based on the data obtained from the laboratory tests, the sandstone layer was assigned the Mohr–Coulomb model and the mudstone layer was assigned the Burgers–Mohr–Coulomb model for calculations. Numerical models with excavation advances of 10, 15, 20, 25, and 30 m were used for the respective calculations. For the model with an excavation advance of 10 m, the excavation time for one advance was 960 h, the time for one step of excavation in one advance was 80 h, the total time taken to complete the excavation of the cavern was 17,280 h (720 days), and the model continued to calculate for 365 days after the excavation was completed. For the model with an excavation advance of 15 m, the excavation time for one advance was 1440 h, the time for one step of excavation in one advance was 120 h, the total time taken to complete the excavation of the cavern was 17,280 h (720 days), and the model continued to calculate for 365 days after the excavation was completed. For the model with an excavation advance of 20 m, the excavation time for one advance was 1920 h, the time for one step of excavation in one advance was 160 h, the total time taken to complete the excavation of the cavern was 17,280 h (720 days), and the model continued to calculate for 365 days after the excavation was completed. For the model with an excavation advance of 25 m, the excavation time for one advance was 2472 h, the time for one step of excavation in one advance was 206 h, the total time taken to complete the excavation of the cavern was 17,280 h (720 days), and the model continued to calculate for 365 days after the excavation was completed. For the model with an excavation advance of 30 m, the excavation time for one advance was 2880 h, the time for one step of excavation in one advance was 240 h, the total time taken to complete the excavation of the cavern was 17,280 h (720 days), and the model continued to calculate for 365 days after the excavation was completed. The mentioned models were shown in Figure 7. For each numerical model, anchor bolt support was performed with each step of excavation and lining support was conducted after the completion of the excavation for each advance. The support parameters for the anchor bolt and lining were the same as presented in Section 2.2.3.
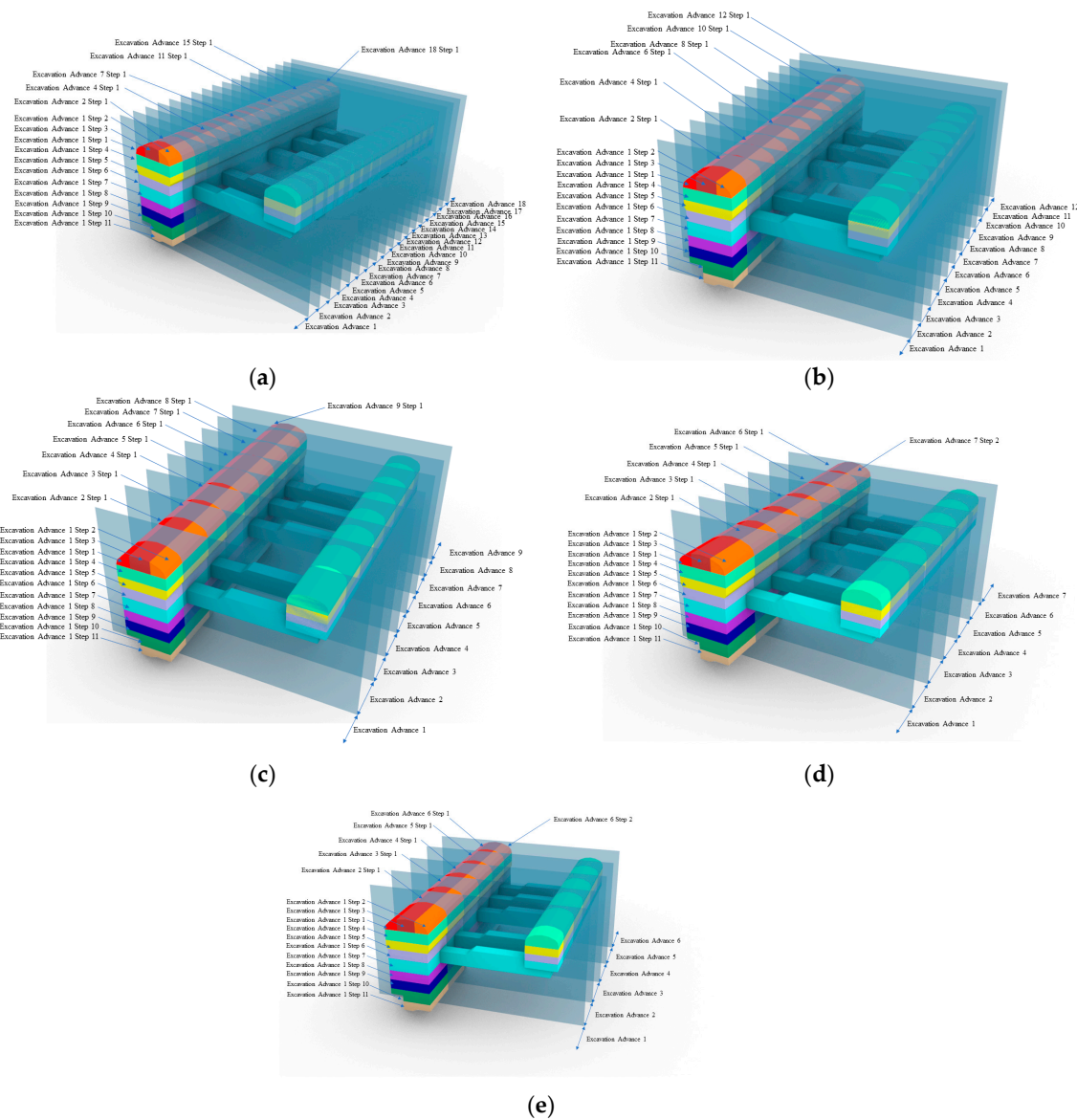
Figure 7. Different excavation advance models. (**a**) Excavation advance: 10 m; (**b**) excavation advance: 15 m; (**c**) excavation advance: 20 m; (**d**) excavation advance: 25 m; (**e**) excavation advance: 30 m.

2.2.5. The Numerical Model for Discussing the Effect of the Lining Thickness on Lining Stress

Based on the optimal excavation advance selected in Section 2.2.4 for the underground cavern, the thickness of the lining during support was assigned values of 0.5, 1, 1.5, 2, 2.5, and 3 m for the calculations, with all other conditions identical to the model presented in Section 2.2.4.

3. Results

3.1. Laboratory Rock Mechanics Testing

3.1.1. Results of Rock Chemical Composition and Mineral Constituents

The rock consisted of mudstone (50%), quartz (30%), calcite (10%), sericite (1%), opaque minerals (1%), and iron matter (8%). The rock exhibited clastic and muddy structures, with a blocky texture. The clastic component constituted about 20% of the rock, composed mainly of calcite and quartz. The interstitial material accounted for approximately 80% and was composed of quartz, mudstone, calcite, sericite, opaque minerals, and iron matter. The cementation in the rock occurred primarily at the base. The clastic quartz had a well-

rounded shape, with grain sizes between 0.03 and 0.04 mm, with a few grains reaching up to 0.2 mm. The interstitial quartz had a size of 0.01 mm. Calcite appeared as a microcrystalline structure, forming irregular, bay-shaped, or round aggregates, with grain sizes between 0.6 and 1 mm. In some grains, the core was microcrystalline calcite and the edge was clayey calcite, while others were entirely clayey calcite. The interstitial calcite had a size of 0.02 mm. Sericite appeared as cement with a fine, scaly shape and a size of 0.01 mm. Opaque minerals acted as cement with irregular shapes and sizes between 0.01 and 0.02 mm. Iron matter appeared as cement with an irregular shape; in some places, it was uniformly impregnated with very-fine particles while, in others, it formed iron cement. The results of the petrographic analysis were shown in Figure 8.
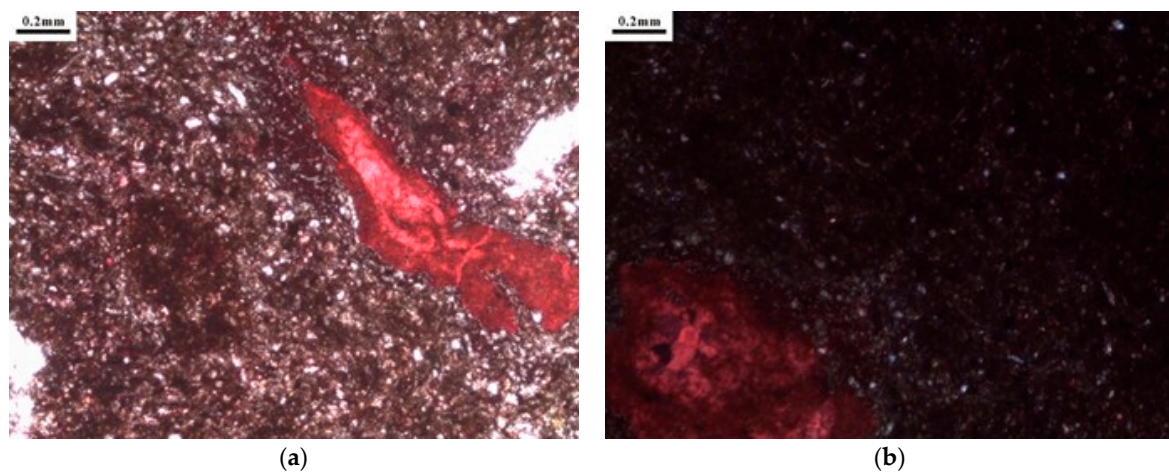

(a)   (b)

Figure 8. Photomicrographs. (**a**) Plane-polarized light; (**b**) cross-polarized light.

3.1.2. Results of Rock Chemical Composition and Mineral Constituents

1.   Uniaxial Compressive Strength Test Results

Table 2 presents the results for the uniaxial compressive strength tests performed on the rock samples. Figure 9a displays the damaged sandstone sample, while Figure 9b shows the failed mudstone sample.

Table 2. Rock physical and mechanical properties' test results.

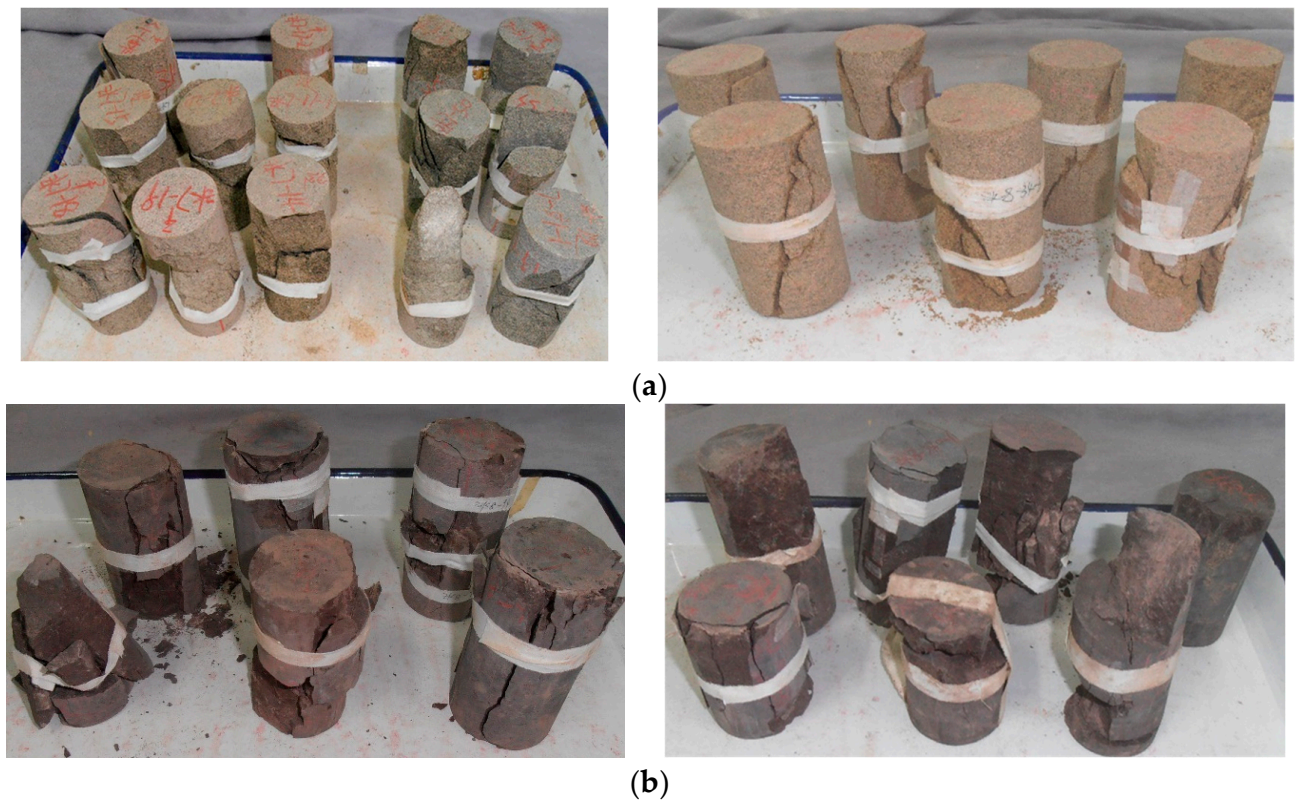| Name	Characteristic	Particle Density ρ_p g/cm³	Saturated Density ρ_s g/cm³	Bulk Dry Density ρ_d g/cm³	Saturated Water Absorption Rate ω_s %	Porosity n %	Saturated Compressive Strength R_s MPa	Dry Compressive Strength R_d MPa	Softening Coefficient η -	Static Elastic Modulus E_e GPa	Poisson's Ratio μ_e -
Sandstone	Samples Range	10 2.64–2.72	10 2.56–2.66	10 2.51–2.63	10 1.35–1.99	2 4.07–4.49	7 46.8–82.0	6 110–136	2 0.44–0.59	6 19.0–31.8	5 0.22–0.25
	Arithmetic mean $\bar{x}$	2.68	2.61	2.57	1.64	4.28	63.6	125	0.52	26.5	0.24
	Standard deviation σ	0.034	0.043	0.048	0.267	-	13.557	10.926	-	5.469	0.011
	Coefficient of variation Cv	0.013	0.016	0.019	0.163	-	0.213	0.087	-	0.206	0.046
	Standard value	2.68	2.61	2.56	1.69	-	59.8	121	-	24.7	0.24
Mudstone	Samples Range	10 2.72–2.78	10 2.59–2.65	10 2.49–2.61	10 1.50–4.21	2 5.84–7.30	6 7.87–24.5	6 36.7–79.6	2 0.24–0.30	6 10.0–18.1	5 0.25–0.30
	Arithmetic mean $\bar{x}$	2.74	2.63	2.56	2.54	6.57	16.7	60.9	0.27	13.5	0.27
	Standard deviation σ	0.017	0.019	0.035	0.699	-	6.309	18.148	-	3.531	0.019
	Coefficient of variation Cv	0.006	0.007	0.014	0.275	—	0.378	0.298	—	0.262	0.072
	Cv	2.74	2.63	2.56	2.67	—	14.6	54.7	—	12.3	0.28

(**a**)

(**b**)

Figure 9. Failure characteristics after uniaxial compressive strength test of the rock. (**a**) Post-test sandstone sample; (**b**) post-test mudstone sample.

2. Shear Test Results

The specimens basically sheared along the rock itself, with a surface roughness difference of 0~2.5 cm. The mudstone surface showed many rock fragments and debris. The cross-sections of the specimens after the test are shown in Figures 10 and 11. The test results are presented in Table 3.
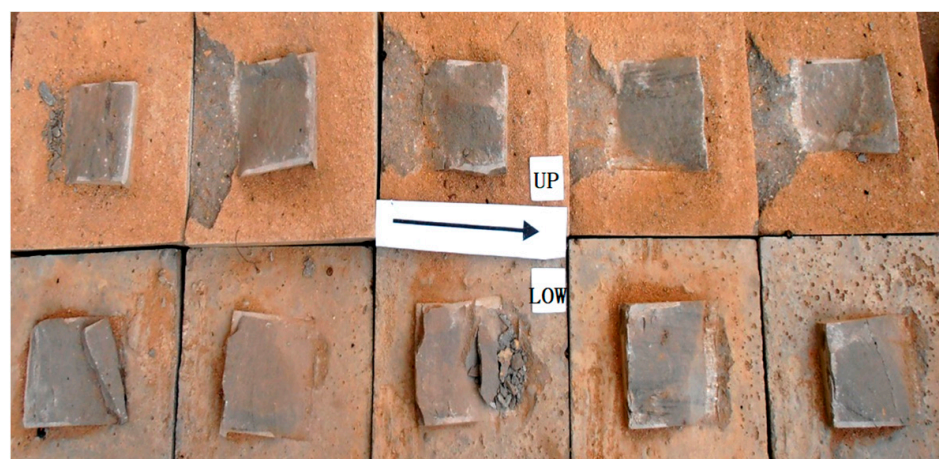

Figure 10. Sandstone post-test sections.

(**a**)   (**b**)

Figure 11. Mudstone post-test sections. (**a**) Before the test; (**b**) after the test.

Table 3. Results of direct shear strength test.

Name	Characteristic	Shear Fracture Test		Shear Test	
		f′ °	c′ MPa	f′ °	c′ MPa
Sandstone	Sample number Range Average	2 1.73~1.76 1.74	2 4.84~5.83 5.34	6 0.73~0.96 0.86	6 0.22~0.57 0.42
Mudstone	Sample number Range Average	4 1.20~1.24 1.22	4 0.93~1.87 1.43	12 0.48~0.74 0.58	12 0.20~0.50 0.31

3.1.3. Creep Test Result for Mudstone

The creep curves under different confining pressures (0.5, 3, and 6 MPa) and water-bearing conditions (natural and saturated) were obtained by data acquisition after loading according to the abovementioned test methods and loading schemes, as shown in Figure 12. Among them, when mudstone was saturated, it was more affected by cracks. In addition, during the test process, the samples would suddenly destabilize and destroy after the first or second pressure-applied steps. This meant that, after the mudstone samples were saturated with water, the mechanical parameters varied greatly.

The failure diagrams of each creep pattern are shown in Figure 13. It can be observed that the failure mode of mudstone after saturation is more controlled by joints.

The stepped rheological deformation curves obtained by the step loading method needed to be processed to form a set of rheological curves at different stress levels, which was convenient for further fitting and obtaining the relevant parameters of the rheological model. A rheological deformation curve is usually processed by the coordinate translation method, i.e., the time of loading at each stage is taken as the time of "0", and then the time is calculated from the time of "0", which is equal to the time moving forward. This treatment assumes that the rock mass is a linear variant. This is the well-known linear Boltzmann superposition principle. Based on the requirements of the linear superposition theory for the creep test, the creep test requires that the loading time of each stage must be consistent and that each stage of loading must continue until the pattern enters the steady-state creep stage. However, this approach ignores the impact of loading history on style.

In this paper, Chen's mapping method was used to process the relevant test data. The advantage of Chen's method was that it could be used as a graphical method to establish the superposition relationship of a real deformation process through appropriate experimental techniques and methods, whether the aftereffect was linear or non-linear, considering the memory effect of real rheological media on the loading history. Chen's plotting method was designed to measure the distance of the sample, as shown in Figure 14a. With a step

loading value of $\Delta\sigma$, the step creep test curves were obtained, as shown in Figure 14b, and the load was deduced to be $\sigma N = n \Delta\sigma$ creep curve under one-off loading.
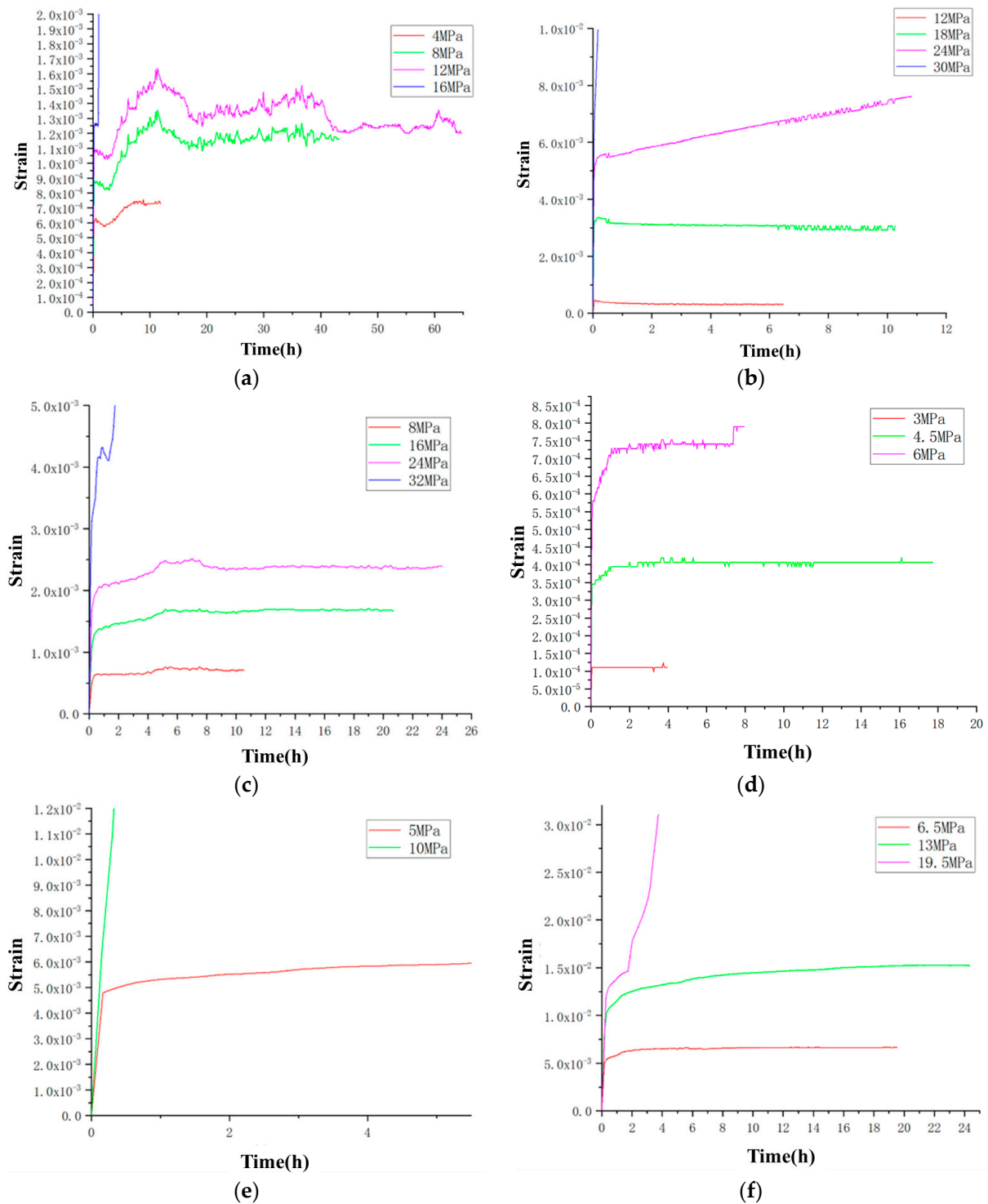

Figure 12. Graded loading creep curve of mudstone. (**a**) Natural-state confining pressure: 0.5 MPa; (**b**) natural-state confining pressure: 3 MPa; (**c**) natural-state confining pressure: 6 MPa; (**d**) saturated ambient pressure: 0.5 MPa; (**e**) saturated ambient pressure: 3 MPa; (**f**) saturated ambient pressure: 6 MPa.
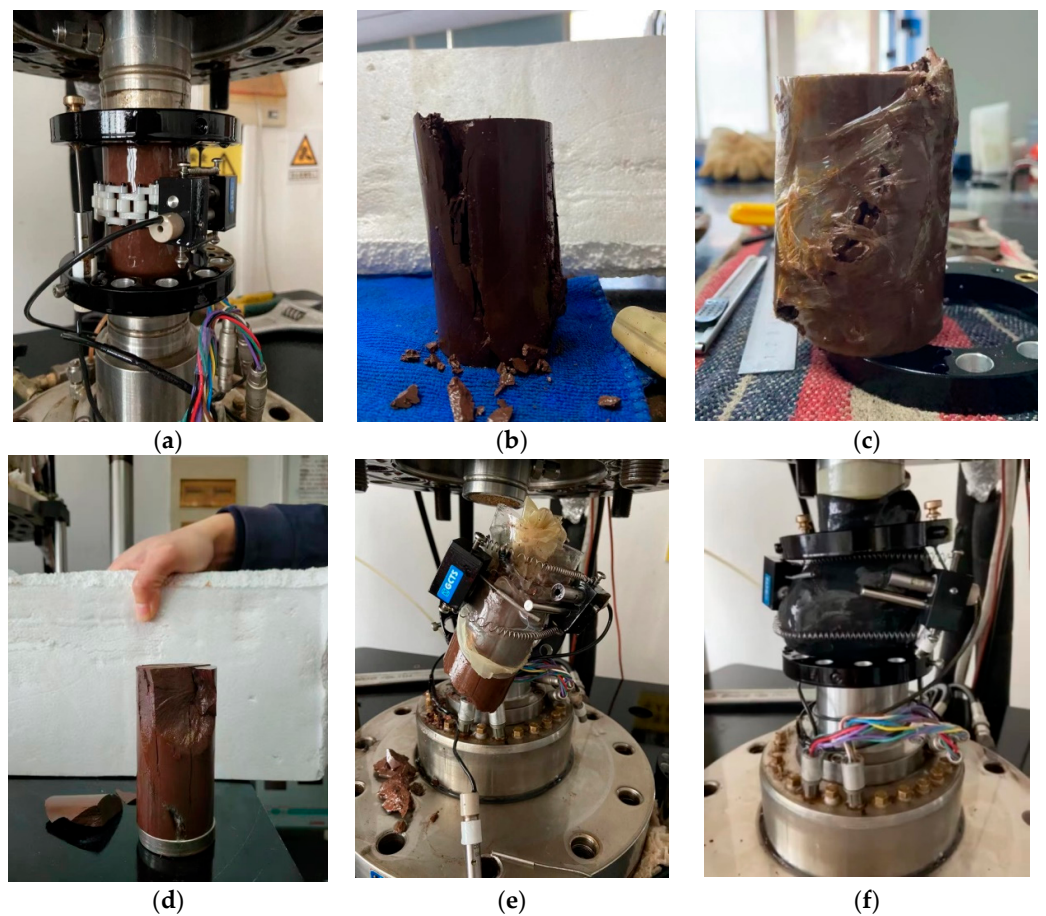
Figure 13. Creep failure characteristics of mudstone samples under different confining pressures. (**a**) Natural state 0.5 MPa; (**b**) Natural state 3 MPa; (**c**) Natural state 6 MPa; (**d**) Saturated state 0.5 MPa; (**e**) Saturated state 3 MPa; (**f**) Saturated state 6 MPa.
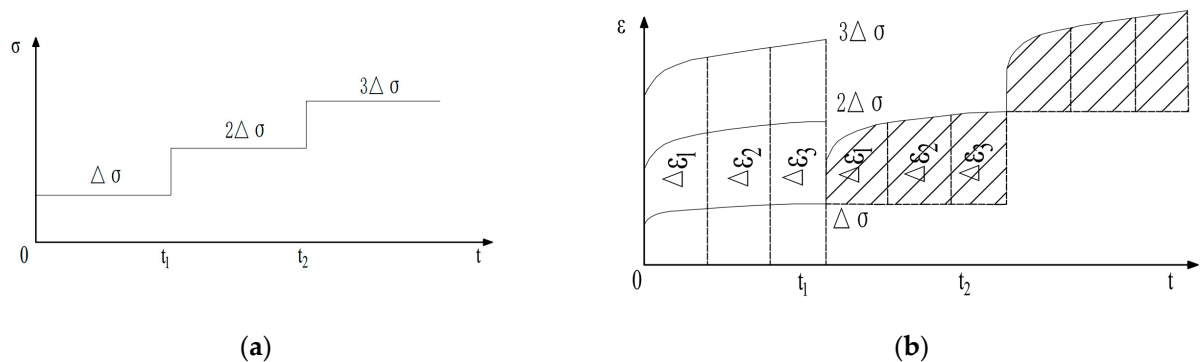

Figure 14. Detailed process of Chen's drawing method. (**a**) step loading; (**b**) step creep experimental curve.

In this method, the test data that reached the stable stage were extended to the corresponding load level with the longest loading time interval as a reference, and the test curves with the shortest loading time interval were extended to the longest time interval according to the slopes of attenuating creep or constant creep. This method can obtain the approximate fitting parameters of the model after reaching the stable creep stage in each stage, ignoring the considerable difference of the time intervals. Figure 15 shows the creep curves under separate loading conditions.
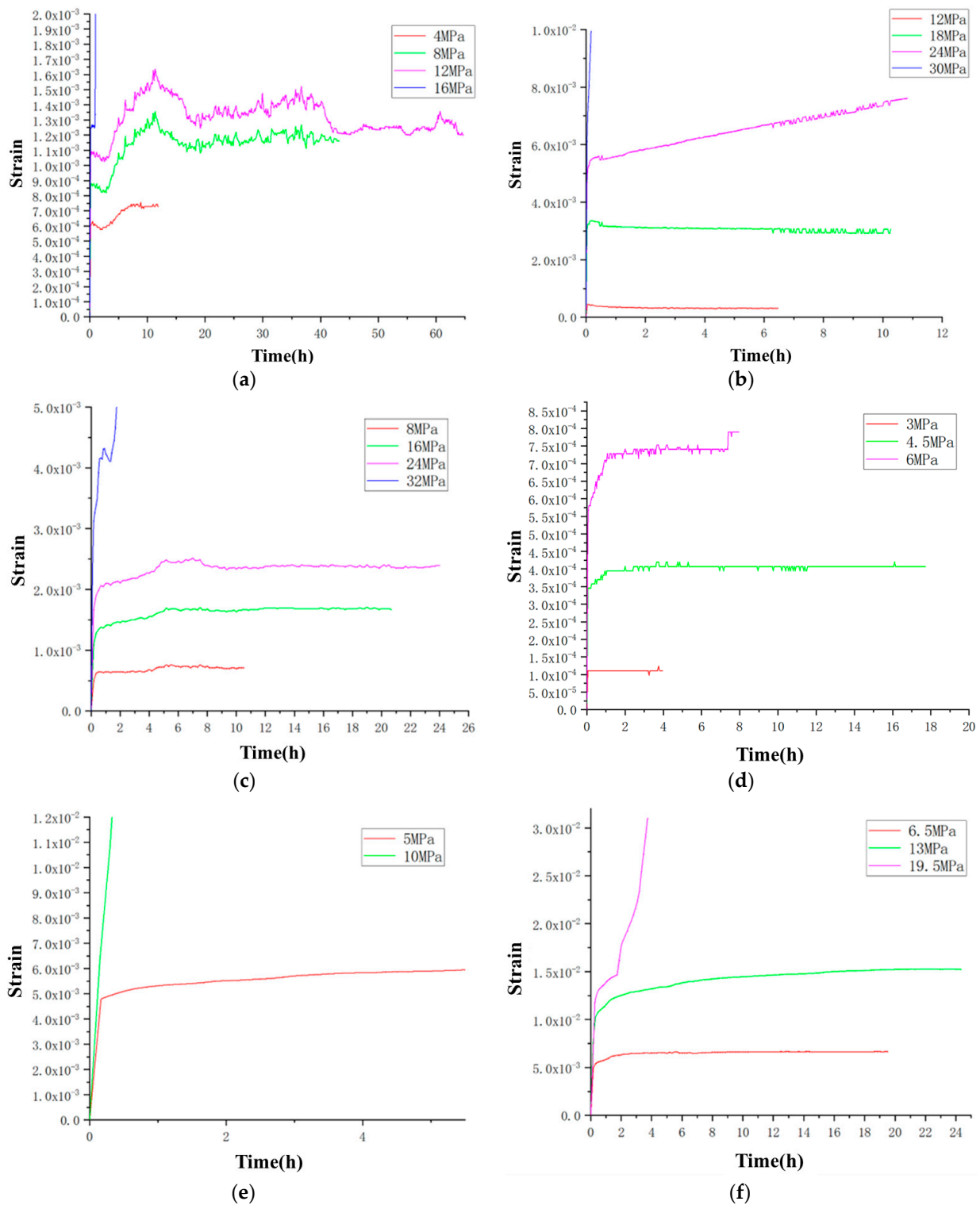
Figure 15. Creep curves under separate loading. (**a**) Natural-state confining pressure: 0.5 MPa; (**b**) natural-state confining pressure: 3 MPa; (**c**) natural-state confining pressure: 6 MPa; (**d**) surrounding pressure in saturated state: 0.5 MPa; (**e**) surrounding pressure in saturated state: 3 MPa; (**f**) surrounding pressure in saturated state: 6 MPa.

3.1.4. Mudstone Creep Parameter Fitting

Mudstone has obvious viscoelastic deformation characteristics. In this study, a series of M–C plastics in the Burgers model were used to form a Burgers–Mohr–Coulomb model.

M–C plastics consist of M–C and plastic bodies in parallel. For M–C plastics, the element is strain-free when the stress level is lower than the stress limit for the Mohr–Coulomb criterion. The element generates an infinite strain when the stress level it is subjected to is higher than the stress limit of its Mohr–Coulomb criterion. Therefore, the Burgers–Mohr–Coulomb model can not only describe the viscoelastic rheological state of rock, but also the accelerated creep failure stage of rock after achieving long-term strength. Therefore, the calculation used the Burgers–Mohr–Coulomb model to describe the creep deformation characteristics of the mudstone and sandstone samples.

Based on the Burgers–Mohr–Coulomb model, the model parameters for the mudstone and sandstone samples were fitted to the rheological curves obtained by the test after treatment by Chen's mapping method. No accelerated creep occurred in the mudstone and sandstone samples when the stress level applied by the sample was low. At this stage, the Burgers–Mohr–Coulomb model was a Burgers model, which contained four model parameters: G_K, G_M, η_K, η_M. The M–C plastics in the Burgers–Mohr–Coulomb model played a controlling role when the stress level applied to the sample was high, including the following model parameters: cohesion c and internal friction angle. The target parameters for this rheological model parameter identification were: G_K, G_M, η_K, η_M, i.e., the shear modulus and viscous coefficient of Kelvin and Maxwell bodies. Formula (1) is the creep equation of the Burgers–Mohr–Coulomb model:

$$\varepsilon = \left\{ \frac{1}{G_M} + \frac{t}{\eta_M} + \frac{1}{G_K}\left[1 - \exp(-\frac{G_K}{\eta_K}t) \right] \right\}\sigma_0 \tag{1}$$

Figures 16–21 show a comparative figure between the fitting curve and actual monitoring. Creep model parameters of natural and saturated mudstone formations are shown in Table 4.
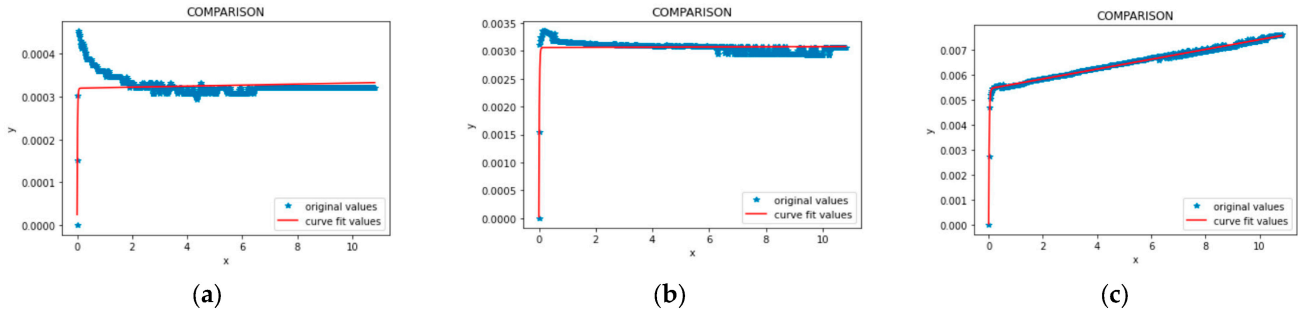

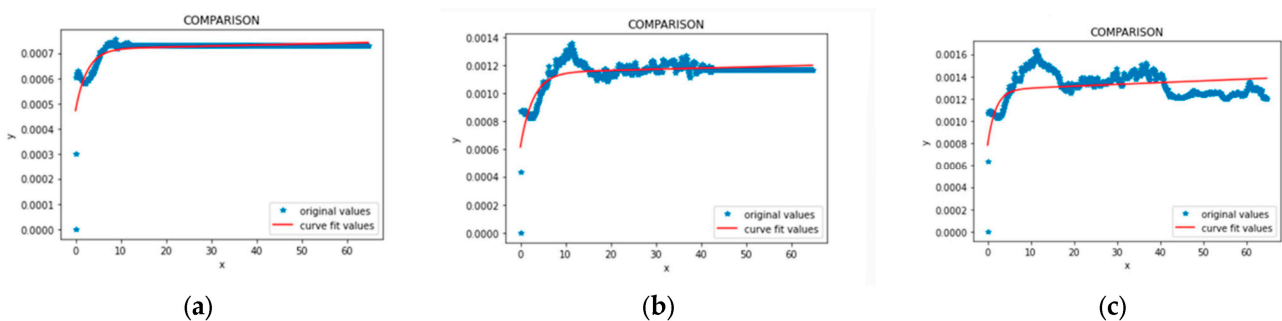**Figure 16.** Fitted parameter diagrams for 0.5 MPa surrounding pressures of mudstone in natural state. (**a**) Phases I; (**b**) II; (**c**) III.

Figure 17. Fitted parameter diagrams for 3 MPa surrounding pressures of mudstone in natural state. (**a**) Phases I; (**b**) II; (**c**) III.
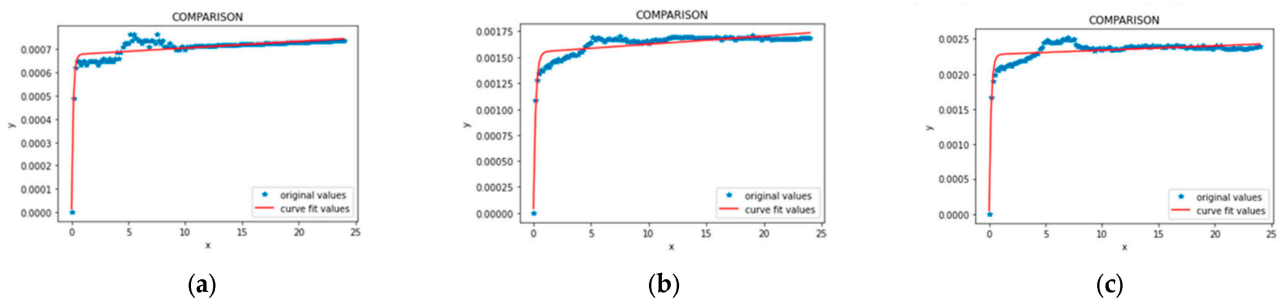
Figure 18. Fitted parameter diagrams for 6 MPa surrounding pressures of mudstone in natural state. (**a**) Phases I; (**b**) II; (**c**) III.
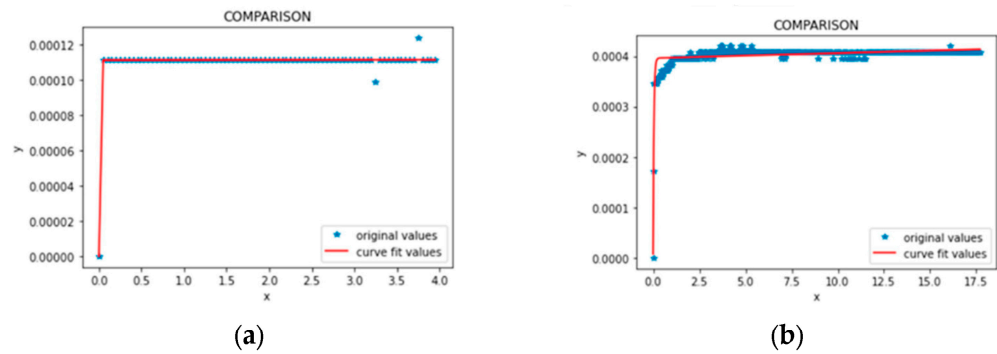

Figure 19. Fitted parameter diagrams for 0.5 MPa surrounding pressures of saturated mudstone. (**a**) Phases I; (**b**) II.
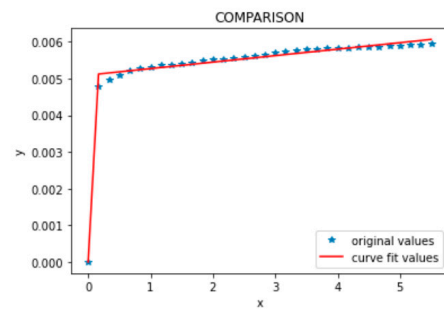

Figure 20. Fitted parameter diagrams for surrounding pressures of saturated mudstone: 3 MPa.
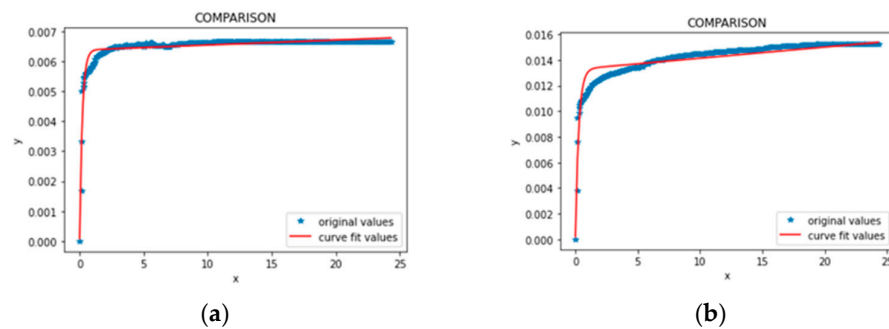

Figure 21. Fitted parameter diagrams for 6 MPa surrounding pressures of saturated mudstone: (**a**) phases I; (**b**) II.

Table 4. Plastic mechanical parameters of surrounding rocks in natural state.

Name	Stress Level (MPa)	G_M (GPa)	G_K (GPa)	η_M (GPa h)	η_K (GPa h)	R^2
Natural 0.5 MPa ambient pressure	4	8.469547	16.43078	10,000	41.99804	0.686724
	8	12.97276	15.10348	10,000	42.17472	0.665318
	12	15.3175	23.43532	10,000	45.79424	0.144663
	Recommended parameters	12.25327	18.32319	10,000	43.32233	
Natural 3 MPa ambient pressure	12	492.7833	40.5884	9999.963	0.585766	0.12463
	18	600	5.940712	10,000	0.09441	0.656332
	24	599.9999	4.435769	121.908	0.092265	0.994597
	Recommended parameters	564.2611	16.98829	6707.29	0.257481	
Natural 6 MPa ambient pressure	8	599.6736	12.07929	2807.976	1.645042	0.89486
	16	368.2403	10.63802	2054.865	1.982264	0.885674
	24	501.1144	10.77981	3832.331	1.781973	0.861349
	Recommended parameters	489.6761	11.16571	2898.391	1.803093	
Saturated 0.5 MPa confining pressure	3	978,118.6	27.02992	49,910.3	0.02233	0.975636
	4.5	599.999	11.58582	4500.291	0.494791	0.80275
	Recommended parameters	489,359.3	19.30787	27,205.29	0.25856	
Saturated 3 MPa confining pressure	6	58,205.47	0.981387	28.28857	0.004189	0.991984
	Recommended parameters	58,205.47	0.981387	28.28857	0.004189	
Saturated 6 MPa confining pressure	6.5	68.61235	1.035484	387.8842	0.217025	0.908607
Saturated 0.5 MPa confining pressure	13	58	0.99652	150	0.265825	0.882436
	Recommended parameters	63.30617	1.016002	268.9421	0.241425	
	3	978,118.6	27.02992	49,910.3	0.02233	0.975636

3.1.5. Parameters Used for the Numerical Model

The test results provide the mechanical parameters for the rock. Considering the development of joints and fissures in the rock mass, the depth of the underground chamber, and the comparison with similar engineering cases, the calculation parameters for mudstone and sandstone in the numerical analysis are shown in Table 5, and the rheological parameters for mudstone are shown in Table 6.

Table 5. Rock physical and mechanical properties used for the numerical model.

Name	Gravity	Dry Density g/cm³	Saturation Water Absorption %	Porosity %	Compressive Strength		Softening Coefficient		Shear Strength	Elastic Modulus	Poisson's Ratio
					Saturated MPa	Dry	f′ °	C′ MPa	GPa	g/cm³	%
Sandstone	2.67	2.45	2.50	6.30	68	100	0.68	1.10	1.20	14.0	0.25
Mudstone	2.76	2.57	2.70	6.88	4	7.5	0.30	0.45	0.10	0.8	0.30

Table 6. Rheological parameters used for the numerical model.

Name	G_M (GPa)	G_K (GPa)	η_M (GPa h)	η_K (GPa h)
Sandstone	489.6761	11.16571	2898.391	1.803093

3.2. The Influence of Support Measures on the Stability of the Surrounding Rock in Underground Caverns

According to the mechanical parameters of the soft-rock mass and the mentioned support methods, the paper discussed the influence of support measures on the stability of the surrounding rock in underground caverns. Therefore, the finite difference method was used to simulate the step-by-step excavation of underground caverns and the displace-

ment trend of the surrounding rock after one year under the condition with or without support measures.

The simulated displacement results of the midspan (y = −79.4 m) of the underground cavern and the whole underground cavern with or without support measures are shown in Figures 22 and 23.
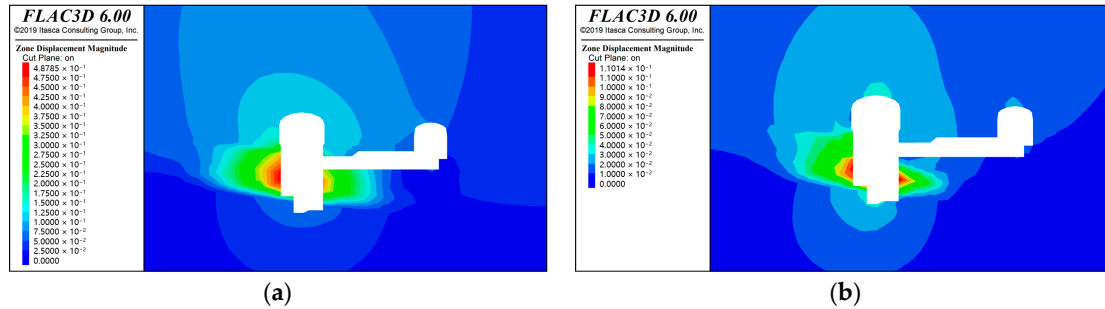

(**a**)

(**b**)

Figure 22. Displacement cloud map of y = −79.4 m section under different support conditions: (**a**) displacement cloud map of y = −79.4 m section under unsupported conditions; (**b**) displacement cloud map of y = −79.4 m section under supported conditions.
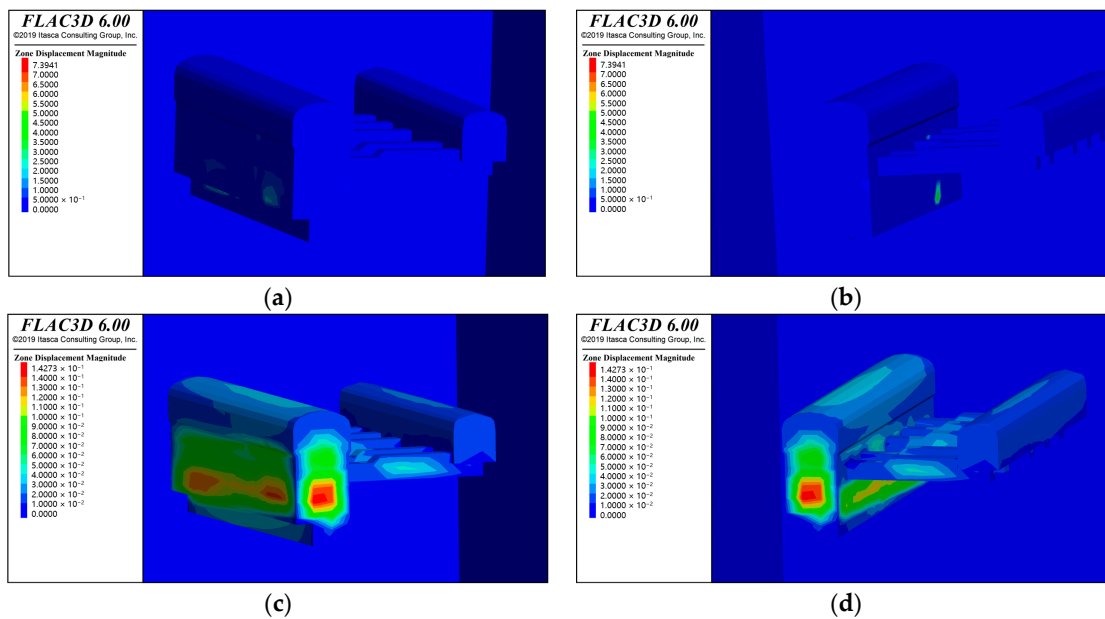

(**a**)

(**b**)

(**c**)

(**d**)

Figure 23. Displacement cloud map of the walls under different support conditions: (**a**) displacement cloud map of the left-side wall under unsupported conditions; (**b**) displacement cloud map of the right-side wall under unsupported conditions; (**c**) displacement cloud map of the left-side wall under supported conditions; (**d**) displacement cloud map of the right-side wall under supported conditions.

According to Figures 22 and 23, it can be observed that, regardless of whether there were support measures or not, the development of deformation in the surrounding rock of the underground caverns was concentrated in the exposed areas of the soft-rock strata, and the displacement of the left wall was greater than that of the right wall. This was because the soft rock was exposed in the middle of the left wall and the lower part of the right wall. The strength of the soft rock was relatively lower compared to the sandstone layer, and the stress release degree was strong. The soft-rock layer on the left wall was in a forward inclined state, while the soft-rock layer on the right wall was in a reverse inclined state. Therefore, the soft-rock layer was a displacement concentration area, and the left wall was more prone to instability compared to the right wall, with a deformation range of the surrounding rock greater than the right wall.

Based on the simulation results and displacement cloud map, the maximum displacement of the left and right walls, the maximum displacement of this section, and the corresponding increment could be obtained. At the same time, the maximum displacement and the increment of the displacement of the whole underground cavern under the conditions with or without support measures could be obtained. The specific displacement values and increments of each part are shown in Table 7.

Table 7. Displacement values and increments of each part under different support conditions.

Location	Support Condition	Maximum Displacement of the Whole Cavern (m)	Maximum Displacement of the Left-Side Wall (m)	Maximum Displacement of the Right-Side Wall (m)
The section of y = −79.4 m	Unsupported condition	0.488	0.488	0.407
	Supported condition	0.110	0.110	0.106
	Increment	−77.46%	−77.46%	−73.96%
The whole underground cavern	Unsupported condition	7.39	/	/
	Supported condition	0.14	/	/
	Increment	−98.11%	/	/

According to the Table 7, it can be observed that, whether the specific section or the whole underground cavern, the maximum displacement under support measures could be effectively reduced. Therefore, the support measure could limit the deformation of the soft rock effectively, reduce the displacement of the surrounding rock efficiently, and improve the stability of the surrounding rock greatly.

In order to understand the influence of the support measures on the displacement of the left- and right-side walls of the underground cavern, three sections were selected from the front, middle, and rear sections (y = −156 m, y = −76 m, y = −30 m) in the excavation direction of the underground cavern, and the maximum horizontal displacement before and after the support of the left- and right-side walls of each section and increments were compared. The maximum horizontal displacement values before and after the support of each section and increments are shown in Table 8, and the displacement cloud diagram is shown in Figure 24.

Table 8. Displacement values and increments of left- and right-side walls in each section under different support conditions.

Location	Support Condition	Maximum Displacement of the Whole Cavern(m)	Maximum Displacement of the Left-Side Wall(m)
Y = −156 m	Unsupported condition	0.525	0.383
	Supported condition	0.119	0.096
	Increment	−77.33%	−74.93%
Y = −76 m	Unsupported condition	0.478	0.388
	Supported condition	0.105	0.112
	Increment	−78.03%	−71.13%
Y = −30 m	Unsupported condition	0.445	0.364
	Supported condition	0.120	0.092
	Increment	−73.03%	−74.73%

According to Figure 24 and Table 8, it can be observed that the displacement of the left-side wall of the cavern under the unsupported condition is greater than that of the right-side wall. However, the displacement of the left-side wall in the front and rear sections of the cavern is still greater than that of the right-side wall, while the displacement of the right-side wall is greater than that of the left-side wall in the midspan of the tunnel. This phenomenon occurred under the influence of the reinforcement effect of anchor rods after support and the stress conduction of the lining.
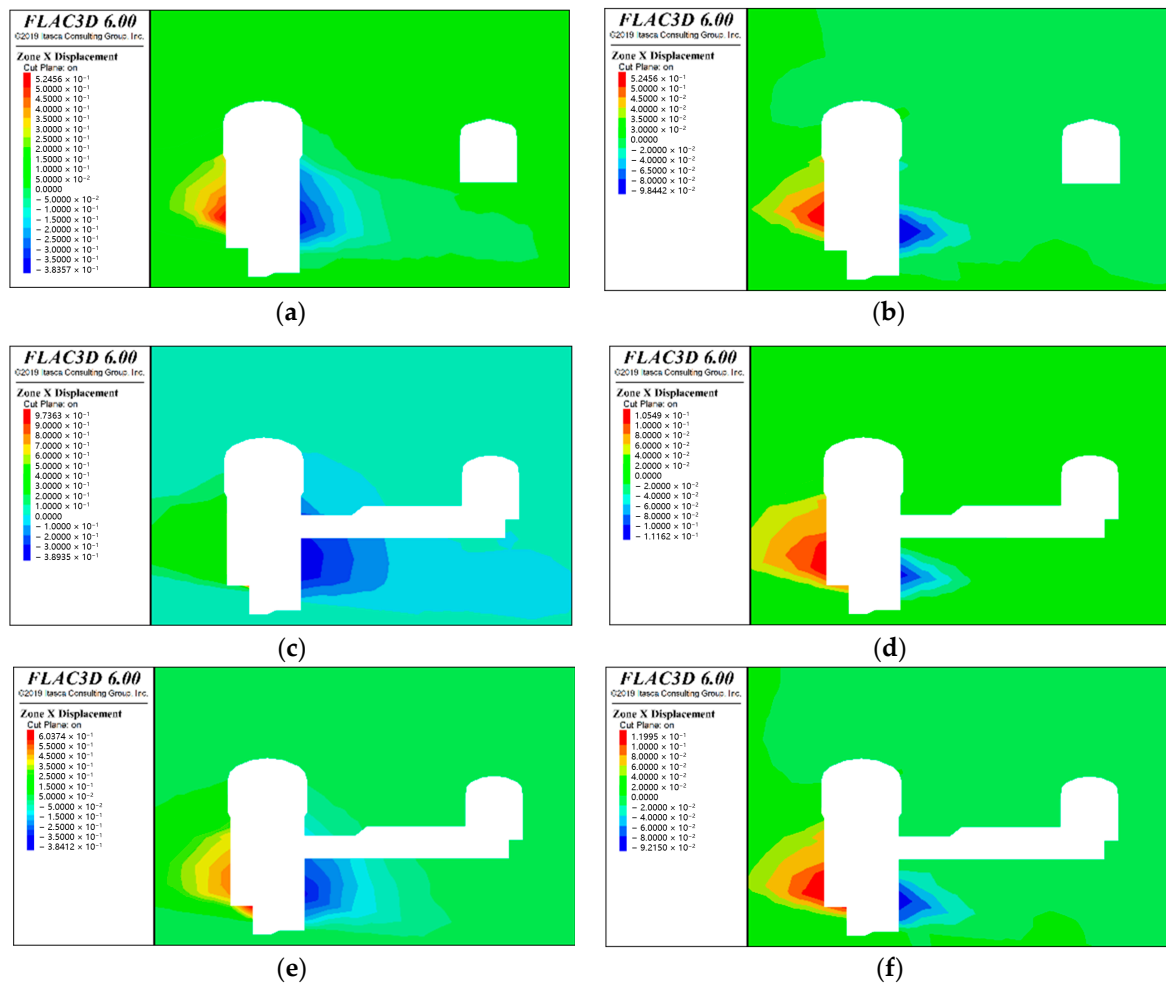
(a)

(b)

(c)

(d)

(e)

(f)

Figure 24. Displacement cloud map of different sections (y = −156 m, −76 m, −30 m) under different support conditions: (**a**) displacement cloud map of y = −156 m section under unsupported conditions; (**b**) displacement cloud map of y = −156 m section under supported conditions; (**c**) displacement cloud map of y = −76 m section under unsupported conditions; (**d**) displacement cloud map of y = −76 m section under supported conditions; (**e**) displacement cloud map of y = −30 m section under unsupported conditions; (**f**) displacement cloud map of y = −30 m section under supported conditions.

3.3. The Influence of Excavation Footage on the Stability of the Surrounding Rock

According to the study presented in Section 3.2, the support measures proposed to improve the stability of the surrounding rock of the underground cavern can limit the deformation of the soft rock effectively and reduce the maximum displacement of each section and the whole underground cavern efficiently. Therefore, using the finite difference method to simulate the step-by-step excavation of underground caverns and the displacement trend of the surrounding rock after one year under different single excavation footage with the support condition is useful. Combining the simulation results and considering the influence of single excavation footage change on the displacement of underground caverns, even more single excavation footage was obtained.

The simulation adopted five types of single excavation footage (10, 15, 20, 25, and 30 m). The maximum displacement value and variables under each single excavation footage schemes are shown in Table 9. The total displacement cloud diagram is shown in Figure 25.

Table 9. The maximum displacement and variables under different single excavation footage schemes.

Length of Single Excavation Footage (m)	Maximum Displacement (m)	Variables of Maximum Displacement (m)
10	0.18774	/
15	0.20121	0.01347
20	0.21074	0.00953
25	0.21252	0.00178
30	0.21424	0.00172

(**a**)

(**b**)

(**c**)

(**d**)

(**e**)
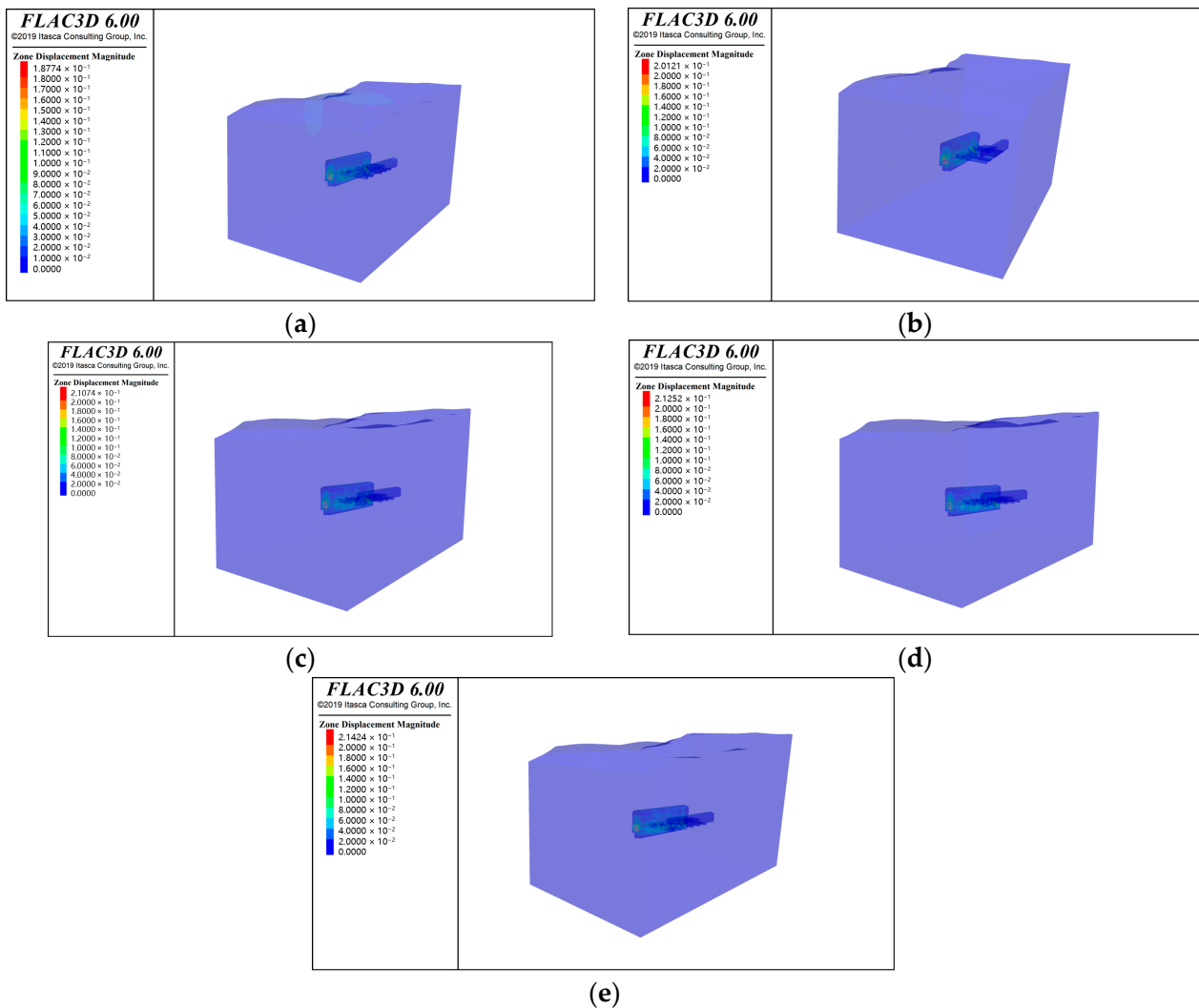
Figure 25. Displacement cloud map of different single excavation footage schemes: (**a**) displacement cloud map of the length of 10 m excavation footage; (**b**) displacement cloud map of the length of 15 m excavation footage; (**c**) displacement cloud map of the length of 20 m excavation footage; (**d**) displacement cloud map of the length of 25 m excavation footage; (**e**) displacement cloud map of the length of 30 m excavation footage.

According to the displacement cloud map and maximum displacement of the underground cavern under different single excavation footage schemes shown in Figure 25 and Table 9, it can be concluded that the deformation of the surrounding rock of the underground cavern increased with the increase in single excavation footage. A comparison of the maximum displacement is shown in Figure 26.
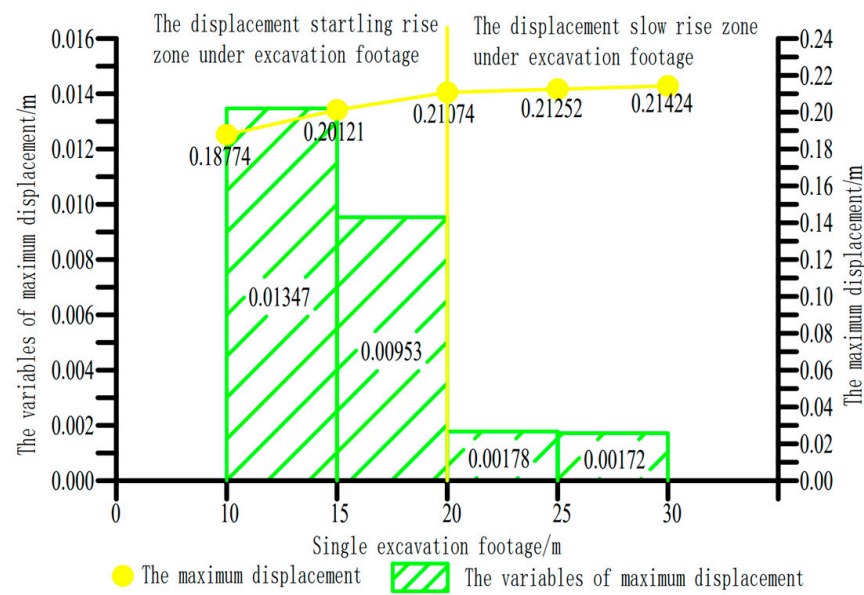
Figure 26. The comparison of the maximum displacement under different single excavation footage schemes.

Based on Figure 23, it can be observed that, although the maximum displacement of the cavern continuously increases with the increase in single excavation footage, the growth rate decreases. When the excavation footage is longer than or equal to 20 m, the maximum displacement growth rate decreases at a relatively stable level, which can ensure the stable changes in the trend of surrounding rock displacement. For this project, considering both the construction duration and the stability of the surrounding rock of the underground cavern, it was proposed to adopt a length of 20 m as the optimal excavation footage.

3.4. The Correlation between Lining Thickness and Stress Variation within the Lining

According to the support method and the optimal excavation footage of 20 m, numerical analyses and calculations were conducted by using the finite difference method based on different lining thicknesses (0.5, 1.0, 1.5, 2.0, 2.5, and 3.0 m), while considering the variation trend of intermediate principal stress of the lining with different thicknesses in the midspan $y = -79.4$ m section of the cavern, choosing the optimal lining thickness. The cloud diagrams of the intermediate principal stress values for different lining thicknesses at the section of $y = -79.4$ m in the cavern are shown in Figure 27, and the maximum intermediate principal stress for each lining thickness is shown in Table 10.

Table 10. The maximum intermediate principal stress for each lining thickness.

Thickness (m)	Maximum Intermediate Principal Stress (Mpa)
0.5	95.6
1.0	72.8
1.5	60.2
2.0	54.6
2.5	53.5
3.0	52.2

According to the middle principal stress cloud diagram and maximum middle principal stress of the $y = -79.4$ m section in the cavern under different thicknesses of lining shown in Figure 27 and Table 10, it can be concluded that the intermediate principal stress in the lining gradually decreases and tends to be stable. The comparison of the maximum intermediate principal stress is shown in Figure 28.
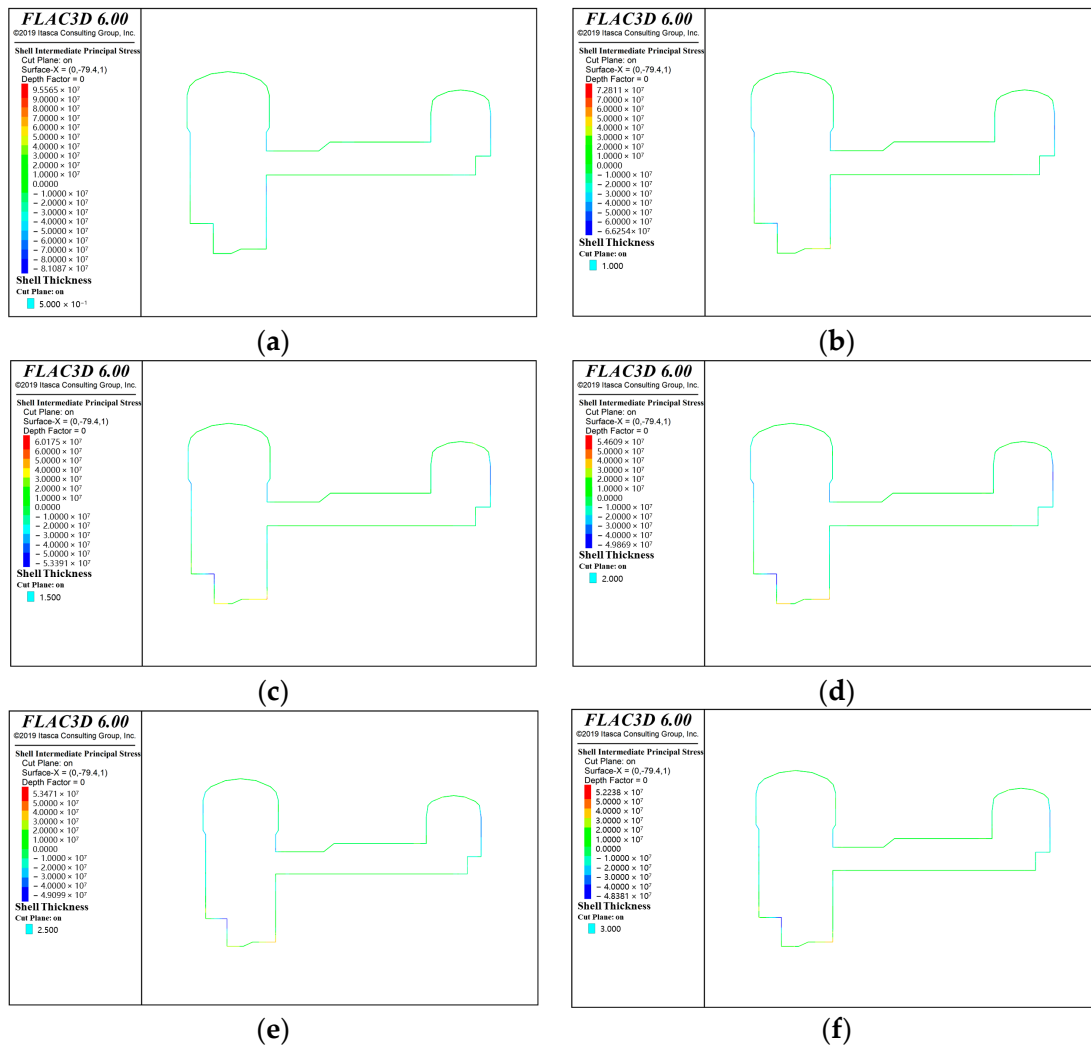
Figure 27. Middle principal stress cloud diagram of different intermediate principal stress values. (**a**) Middle principal stress cloud diagram of 0.5 m lining; (**b**) middle principal stress cloud diagram of 1.0 m lining; (**c**) middle principal stress cloud diagram of 1.5 m lining; (**d**) middle principal stress cloud diagram of 2.0 m lining; (**e**) middle principal stress cloud diagram of 2.5 m lining; (**f**) middle principal stress cloud diagram of 3.0 m lining.

Figure 28. The comparison of the maximum intermediate principal stress under different lining thicknesses.

As shown in Figure 28, an increase in the lining thickness can effectively reduce the maximum intermediate principal stress. When the thickness is less than 2.0 m, the change in thickness has a significant influence on the stress reduction, whereas when the thickness is greater than 2.0 m, the change in thickness has a reduced influence on the stress reduction. Therefore, we adopted a lining thickness of 1.5 m as the optimal size, which could effectively reduce the lining stress and meet the safety requirements while ensuring good economical outcomes.

4. Conclusions

1. Through a petrographic analysis, uniaxial compressive strength tests, and shear tests, the basic engineering characteristics of the study stratum were identified. Subsequently, the stress–strain curves of mudstone in natural and saturated states under different surrounding rocks at 0.5, 3, and 6 MPa were obtained through triaxial creep tests, and the relevant calculation parameters were fitted according to the constitutive equation.

2. By analyzing the calculation results for the cavern excavation under the conditions of support and no support, it can be observed that the maximum deformation area of the cavern surrounding rock was located in the exposed area of the soft-rock stratum on the left side of the cavern. This was because, on the left side of the cavern, the stratum was inclined, while on the right side of the cavern, the stratum was a reverse inclined stratum, which meant that the main control factor of the cavern's surrounding rock was the distribution of the soft rock in the composite stratum. Then, we observed that, under the condition of no support, the displacement of the left wall was greater than that of the right wall, while under the condition of support, in the position across the center of the underground cavern, the displacement of the right wall was greater than that of the left wall, that is, the support measures lead to the offset of the maximum displacement area.

3. Through the research conducted on five different excavation distances of 10, 15, 20, 25, and 30 m, we found that as the excavation advance increased, the deformation of the surrounding rock also gradually increased; however, the growth rate of the surrounding rock deformation decreased. This can be clearly divided into the rapid and slow increase areas of the surrounding rock's deformation. The shorter the excavation footage, the better the stability of the surrounding rock. However, beyond a certain range, the increase in excavation footage would have less of an impact on the stability of the surrounding rock.

4. Based on the single excavation advance of 20 m, the support was conducted with linings of 0.5, 1.0, 1.5, 2.0, 2.5, and 3.0 m. By comparing the maximum intermediate principal stress and the variation in the intermediate principal stress under different lining thicknesses, it was found that the increase in the lining thickness reduced the lining stress, and with the increase in thickness, the stress reduction could be clearly divided into two parts: the effective stress reduction area and the low-efficiency stress reduction area. Therefore, for the lining, the increase in the lining thickness could effectively reduce the pressure on the lining at the initial stage of the thickness increase. After a certain thickness level was exceeded, the change in the lining thickness had little effect on the pressure on the lining. Considering the economic benefits comprehensively, a lining thickness of 1.5 m was chosen as the optimal lining thickness value.

Author Contributions: Investigation resources and validation, N.S., S.L., D.H., M.H., Z.L. and F.Z.; writing, N.S., X.L., M.D. and Z.L.; software, X.L., S.L.; Z.L. and Y.Z.; creep test, Z.L. All authors have read and agreed to the published version of the manuscript.

Data Availability Statement: The data for this study was designed for a nationally important hydroelectric facility, so we are sorry that we cannot provide public data.

References

1. Zhao, B.-Y.; Ma, Z.-Y. Influence of Cavern Spacing on the Stability of Large Cavern Groups in a Hydraulic Power Station. *Int. J. Rock Mech. Min. Sci.* **2009**, *46*, 506–513. [CrossRef]
2. Huang, X.; Yu, C.; Ma, H. Numerical Study of the Influence of Interlayer Mechanical Properties on Salt Cavern Storage Stability. In *Applied Mechanics and Civil Engineering II*; Xie, L., Ed.; Trans Tech Publications Ltd.: Bach, Switzerland, 2012; Volume 188, pp. 66–71. (In Chinese)
3. Xue, Y.G.; Li, S.C.; Qiu, D.H.; Wang, Z.C.; Su, M.X.; Tian, H. Classification Model of Surrounding Rock of Underground Oil Storage Caverns Based on Weights Back Analysis Method and Efficacy Coefficient Method and Its Application. *Rock Soil Mech.* **2013**, *34*, 3549–3554. (In Chinese)
4. Tsesarsky, M.; Gal, E.; Machlav, E. 3-D Global-Local Finite Element Analysis of Shallow Underground Caverns in Soft Sedimentary Rock. *Int. J. Rock Mech. Min. Sci.* **2013**, *57*, 89–99. [CrossRef]
5. Zhou, Y.; Wu, L.; Li, J.; Yuan, Q. The Effect of Blast-Induced Vibration on the Stability of Underground Water-Sealed Gas Storage Caverns. *Geosyst. Eng.* **2018**, *21*, 326–334. [CrossRef]
6. Lu, C.Z.; Sun, Y.L. A Generalized SMP Criterion for the Optimal Support of Soft Rock Tunnel and Its Comparative Analysis. *Rock Soil Mech.* **2016**, *37*, 1956–1962+2020. (In Chinese) [CrossRef]
7. Zhang, X.T.; Zhang, Q.Y.; Xiang, W.; Gao, Q.; Yuan, S.B.; Wang, C. Model Test Study of Zonal Disintegration in Deep Layered Jointed Rock Mass. *Rock Soil Mech.* **2014**, *35*, 2247–2254. (In Chinese)
8. Mortazavi, A.; Nasab, H. Analysis of the Behavior of Large Underground Oil Storage Caverns in Salt Rock. *Int. J. Numer. Anal. Methods Geomech.* **2017**, *41*, 602–624. [CrossRef]
9. Zhang, G.; Wang, L.; Wu, Y.; Li, Y.; Yu, S. Failure Mechanism of Bedded Salt Formations Surrounding Salt Caverns for Underground Gas Storage. *Bull. Eng. Geol. Environ.* **2017**, *76*, 1609–1625. [CrossRef]
10. Zhang, G.; Liu, Y.; Wang, T.; Zhang, H.; Wang, Z.; Zhao, C.; Chen, X. Pillar Stability of Salt Caverns Used for Gas Storage Considering Sedimentary Rhythm of the Interlayers. *J. Energy Storage* **2021**, *43*, 103229. [CrossRef]
11. Sun, X.; Chen, F.; Miao, C.; Song, P.; Li, G.; Zhao, C.; Xia, X. Physical Modeling of Deformation Failure Mechanism of Surrounding Rocks for the Deep-Buried Tunnel in Soft Rock Strata during the Excavation. *Tunn. Undergr. Space Technol.* **2018**, *74*, 247–261. [CrossRef]
12. Liu, J.; Zhu, Z.H.; Wu, H.; Zhang, S.L.; Wang, J.M. Study of Deformation Characteristics of the High Sidewall Surrounding Rock in Super Large Underground Caverns. *Rock Soil Mech.* **2019**, *40*, 4030–4040.
13. Merlini, D.; Stocker, D.; Falanesca, M.; Schuerch, R. The Ceneri Base Tunnel: Construction Experience with the Southern Portion of the Flat Railway Line Crossing the Swiss Alps. *Engineering* **2018**, *4*, 235–248. [CrossRef]
14. Meng, X.-R.; Peng, R.; Zhao, G.-M.; Li, Y.-M. Roadway Engineering Mechanical Properties and Roadway Structural Instability Mechanisms in Deep Wells. *KSCE J. Civ. Eng.* **2018**, *22*, 1954–1966. [CrossRef]
15. Wang, Z.; Liu, Z.; Ma, W.; Shi, S.; Bu, L. Calculation Method of Underground Cavern Loosening Pressure Based on Limit Analysis Using Upper-Bound Theory and Its Engineering Application. *Math. Probl. Eng.* **2020**, *2020*, 5096931. [CrossRef]
16. Rybak, J.M.; Kongar-Syuryun, C.; Tyulyaeva, Y.; Khayrutdinov, A.M.; Akinshin, I. Geomechanical Substantiation of Parameters of Technology for Mining Salt Deposits with a Backfill. *Min. Sci.* **2021**, *28*, 19–32. [CrossRef]
17. Dyduch, G.; Jarczyk, P.; Jendryś, M. Geomechanical Analysis of the Rock Mass Stability in the Area of the "Regis" Shaft in the "Wieliczka" Salt Mine. In *Minefill 2020–2021*; CRC Press: Boca Raton, FL, USA, 2021; pp. 349–359.
18. Li, G.; Hu, Y.; Tian, S.; Weibin, M.; Huang, H. Analysis of Deformation Control Mechanism of Prestressed Anchor on Jointed Soft Rock in Large Cross-Section Tunnel. *Bull. Eng. Geol. Environ.* **2021**, *80*, 9089–9103. [CrossRef]
19. Zheng, H.; Bragard, C.; Calvo, C.H.; Mooney, M.; Gutierrez, M. Observed Performance and Analysis of SEM Cavern Construction in Downtown Los Angeles. *J. Geotech. Geoenviron. Eng.* **2021**, *147*, 05021011. [CrossRef]
20. Rybak, J.; Khayrutdinov, M.M.; Kuziev, D.A.; Kongar-Syuryun, C.B.; Babyr, N.V. Prediction of the Geomechanical State of the Rock Mass When Mining Salt Deposits with Stowing. *J. Min. Inst. Zap. Gorn. Inst.* **2022**, *253*, 61–70. [CrossRef]
21. Sari, M. Two- and Three-Dimensional Stability Analysis of Underground Storage Caverns in Soft Rock (Cappadocia, Turkey) by Finite Element Method. *J. Mt. Sci.* **2022**, *19*, 1182–1202. [CrossRef]
22. Yang, J.; Qiao, L.; Li, C. Rock Quality Classification Method of Carbonaceous Mudstone Roadway Considering the Influence of Groundwater. *Fresenius Environ. Bull.* **2022**, *31*, 9083–9092.
23. Xie, S.; Jiang, Z.; Chen, D.; Wang, E. Study on Zonal Cooperative Control Technology of Surrounding Rock of Super Large Section Soft Rock Chamber Group Connected by Deep Vertical Shaft. *Adv. Civ. Eng.* **2022**, *2022*, 4220998. [CrossRef]

24. Cui, L.; Sheng, Q.; Zheng, J.; Xie, M.; Liu, Y. A Unified Deterioration Model for Elastic Modulus of Rocks with Coupling Influence of Plastic Shear Strain and Confining Stress. *Rock Mech. Rock Eng.* **2022**, *55*, 7409–7420. [CrossRef]
25. Chen, L.; Wang, Z.; Wang, W.; Zhang, J. Study on the Deformation Mechanisms of the Surrounding Rock and Its Supporting Technology for Large Section Whole Coal Cavern Groups. *Processes* **2023**, *11*, 891. [CrossRef]
26. Mahmoudi, M.; Rajabi, A.M. A Numerical Simulation Using FLAC3D to Analyze the Impact of Concealed Karstic Caves on the Behavior of Adjacent Tunnels. *Nat. Hazards* **2023**, *117*, 555–577. [CrossRef]
27. Zheng, H.; Feng, X.-T.; Hao, X. A Creep Model for Weakly Consolidated Porous Sandstone Including Volumetric Creep. *Int. J. Rock Mech. Min. Sci.* **2015**, *78*, 99–107. [CrossRef]
28. Wei, H.; Xu, W.; Wei, C.; Meng, Q. Influence of Water Content and Shear Rate on the Mechanical Behavior of Soil-Rock Mixtures. *Sci. China-Technol. Sci.* **2018**, *61*, 1127–1136. [CrossRef]
29. Tang, H.; Duan, Z.; Wang, D.; Dang, Q. Experimental Investigation of Creep Behavior of Loess under Different Moisture Contents. *Bull. Eng. Geol. Environ.* **2020**, *79*, 411–422. [CrossRef]
30. Liu, X.; Yang, C.; Yu, J. The Influence of Moisture Content on the Time-Dependent Characteristics of Rock Material and Its Application to the Construction of a Tunnel Portal. *Adv. Mater. Sci. Eng.* **2015**, *2015*, e725162. [CrossRef]
31. Wang, X.K.; Xia, C.C.; Zhu, Z.M.; Xie, W.B.; Song, L.B.; Han, G.S. Long-Term Creep Law and Constitutive Model of Extremely Soft Coal Rock Subjected to Single-Stage Load. *Rock Soil Mech.* **2021**, *42*, 2078–2088. (In Chinese)